ORIGINAL PAPER

Naphthalene-based bis-*N*-salicylidene aniline dyes: Crystal structures, Hirshfeld surface analysis, computational study and molecular docking with the SARS-CoV-2 proteins

Tatyana M. Burkhanova[1,2] · Maria G. Babashkina[3] · Tugba Taskin-Tok[4,5] · Artem V. Sharov[2] · Damir A. Safin[1,2,6]

Abstract
In this work, we report structural and computational studies of a series of naphthalene-based bis-*N*-salicylidene aniline dyes, namely *N*,*N*′-bis-salicylidene-1,5-diaminonaphthalene (**1**), *N*,*N*′-bis(3-hydroxysalicylidene)-1,5-diaminonaphthalene (**2**) and *N*,*N*′-bis(3-methoxysalicylidene)-1,5-diaminonaphthalene (**3**). For **3**, two polymorphs are known, namely **3red** and **3yellow**. Both polymorphs of **3** were analyzed and discussed. All the molecules adopt an enol-imine tautomer, stabilized by two intramolecular O–H···N hydrogen bonds. The structure of **2** is further stabilized by a couple of additional O–H···O hydrogen bonds and by intermolecular O–H···O interactions, yielding a 1D zig-zag supramolecular chain. Molecules of **2**, **3red** and **3yellow** are interlinked through intermolecular C–H···π interactions, while the crystal packing of **1** and **2** is also described by intermolecular π···π interactions. More than 90% of the total Hirshfeld surface area for all the discussed molecules is occupied by H···H, H···C, H···O and C···C contacts. The polymorphs **3red** and **3yellow**, despite being chemically the same, differ geometrically, thus yielding remarkably different Hirshfeld surfaces. The Hirshfeld surface of **3yellow** is very similar to that of **2**. All structures are mainly characterized by the dispersion energy framework followed by the less significant electrostatic energy framework contribution. Molecular docking studies were employed to inspect the effect of **1–3** on the SARS-CoV-2 protein targets. The docking analysis revealed that the dye **2** showed the best binding energies toward Papain-like protease (PLpro, –10.40 kcal/mol), nonstructural protein 14 (nsp14 (N7-MTase), –10.10 kcal/mol), RdRp-RTP (–9.70 kcal/mol) and nonstructural protein 3 (nsp3_range 207-379-MES, –9.30 kcal/mol). The obtained results can give an insight into chemical and biological activities of the studied molecules that could aid in designing of potent reagents SARS-CoV-2.

Keywords *N*-salicylidene aniline dye · Crystal structure · Hirshfeld surface analysis · Molecular docking · SARS-CoV-2 proteins

✉ Tugba Taskin-Tok
ttaskin@gantep.edu.tr

✉ Damir A. Safin
damir.a.safin@gmail.com

[1] University of Tyumen, Volodarskogo Str. 6, Tyumen, Russian Federation 625003

[2] Advanced Materials for Industry and Biomedicine laboratory, Kurgan State University, Sovetskaya Str. 63/4, Kurgan, Russian Federation 640020

[3] Institute of Condensed Matter and Nanosciences, Université Catholique de Louvain, Place L. Pasteur 1, 1348 Louvain-la-Neuve, Belgium

[4] Department of Chemistry, Faculty of Arts and Sciences, University of Gaziantep, 27310 Gaziantep, Turkey

[5] Department of Bioinformatics and Computational Biology, Institute of Health Sciences, University of Gaziantep, 27310 Gaziantep, Turkey

[6] Innovation Center for Chemical and Pharmaceutical Technologies, Ural Federal University named after the First President of Russia B.N. Eltsin, Mira Str. 19, Ekaterinburg, Russian Federation 620002

Introduction

Since Schiff bases $R^1R^2C=NR^3$ ($R^3 \neq H$) were first discovered more than one and a half century ago [1], this type of compounds has, most likely, become the most widely used ligands in chemistry. Schiff bases are readily obtained through condensation of the NH_2 group (primary amine) with the $C(H)=O$ group (aldehyde), yielding secondary aldimines $R^1R^2C=NR^3$ (R^1 or $R^2 = H$, $R^3 \neq H$), or the $R^1R^2C=O$ group (ketone), yielding secondary ketimines $R^1R^2C=NR^3$ ($R^3 \neq H$). The former type is also known as azomethines.

One of the most famous class of Schiff bases is the so-called anils (*N*-phenyl imines), which are produced from aniline or its derivatives [2, 3]. Notably, salicylaldehyde-derived Schiff bases, due to the *ortho*-situated OH group, is one of the most fascinating family. This OH group dictates the possible tautomerization between the enol-imine and keto-enamine isomers, of which the latter one can exhibit either the *cis*- or *trans*-isomers (Scheme 1) [4–13]. Furthermore, this type of Schiff bases is well recognized for their broad color panel, varying from colorless through yellow to red, which is caused by the mentioned isomers (Scheme 1). The formation of a certain isomer, thus yielding different colors, can be dictated by stimuli such as irradiation, temperature and solvent. [4–13]. Nowadays, this feature becomes of great importance for optical devices [14] and molecular switches displaying (ir)reversible stimuli-induced color change in solid state [15]. In this regard, the salicylaldehyde-derived Schiff bases play a pivotal role due to their ease of synthesis, modification and a rich variety of optical properties, also in the solid state.
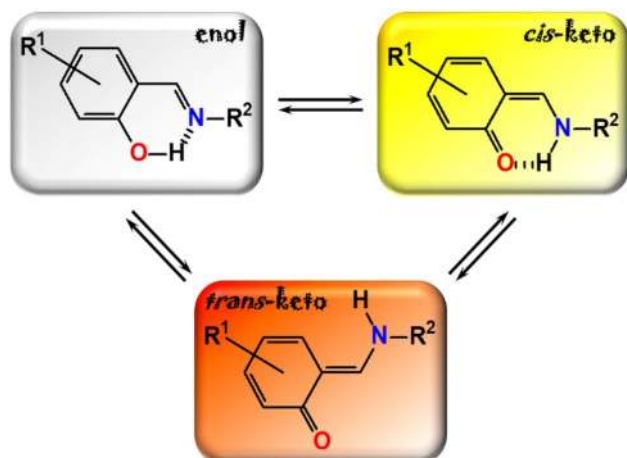
Solid-state optical properties (chromic properties) of the salicylaldehyde-derived Schiff bases are, obviously, dictated by their crystal structure, viz. geometry of a molecule, crystal packing, available free space around the switching unit, flexibility of the nearby environment, etc. [4–13]; thus, the so-called non-covalent interactions formed by this type of molecules become of great importance and therefore are worth to be studied in detail. This becomes even more important for the salicylaldehyde-derived Schiff bases with two or more functional fragments, i.e., obtained from polyamines and/or polyaldehydes.

In this work, in continuation of our ongoing interest to the salicylaldehyde-derived Schiff bases [16–26], we have directed our attention to an extremely rare family of naphthalene-based bis-*N*-salicylidene aniline dyes. Particularly, three dyes, namely *N*,*N*′-bis-salicylidene-1,5-diaminonaphthalene (**1**) [27], *N*,*N*′-bis(3-hydroxysalicylidene)-1,5-diaminonaphthalene (**2**) [28] and *N*,*N*′-bis(3-methoxysalicylidene)-1,5-diaminonaphthalene (**3**) (Fig. 1) [23, 28], which CIF files were subtracted from the Cambridge Structural Database (CSD; CCDC numbers 834421 for **1**, 847259 for **2**, 881637 for **3red** and 881638 for **3yellow**) [29], were subjected for an in-depth structural analysis. Notably, a comprehensive search in the CSD yielded one more crystal structure of the naphthalene-based bis-*N*-salicylidene aniline dye, fabricated from 3,5-di-*tert*-butylsalicylaldehyde [30]. However, the crystal structure of this compound was obtained as an acetone–dimethyl sulfoxide solvate with highly disordered solvent molecules, and thus, it was not considered herein. Recently, some of us have also established that the as-synthesized Schiff base **3** forms red crystals (**3red**), recrystallization of which from acetone produces yellow

Scheme 1 Isomeric forms of *N*-salicylidene aniline derivatives and their color panel
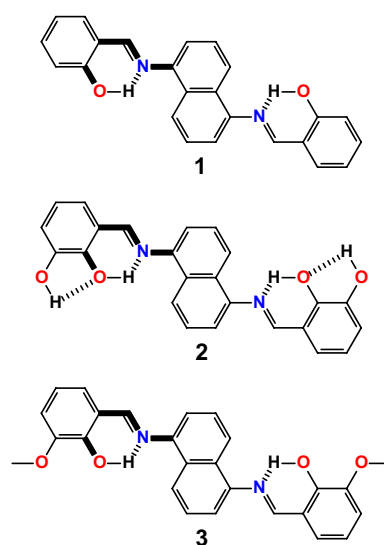
Fig. 1 Diagrams of the discussed Schiff base dyes **1–3**

crystals (**3yellow**). This solvent-induced interconversion is reversible and reproducible, yielding different photophysical properties [23]. Thus, both polymorphs of the Schiff base **3** were analyzed and discussed.

In this work, we focused on detailed studies of crystal structures of **1**, **2**, **3red** and **3yellow** using Hirshfeld surface analysis with the aim to shed more light on non-covalent interactions. Furthermore, energy frameworks have been calculated to analyze the overall crystal packing of these compounds. Besides the above studies, molecular docking studies, which are driven by intermolecular non-covalent interactions, were used to explore the binding modes and interactions of the compounds **1–3** with binding sites of the SARS-CoV-2 proteins as targets at the atomic level. It should be noted that the salicylaldehyde-derived Schiff bases were found to be of interest as antiviral agents against coronavirus [31].

Experimental

Hirshfeld surface analysis

The Hirshfeld molecular surfaces [32] and their associated 2D fingerprint plots [33] were generated using the Crystal-Explorer 17 software [34] on the basis of crystal structures. The d_{norm} (normalized contact distance) surface and the breakdown of the 2D fingerprint plots were used for decoding and quantifying the intermolecular interactions in the crystal lattice. The d_{norm} is a symmetric function of distances to the surface from the nuclei inside (d_i) and outside (d_e) the Hirshfeld surface, relative to their respective van der Waals radii. 2D fingerprint plots were generated using d_i and d_e in the translated 0.4–3.0 Å range and including reciprocal contacts as a pair of coordinates in 2D plots. A color gradient in the fingerprint plots ranging from blue to red is used to visualize the proportional contribution of contact pairs in the global surface.

Enrichment ratio

The enrichment ratio (E) [35] of a pair of elements (X,Y) is the ratio between the proportion of actual contacts in the crystal and the theoretical proportion of random contacts. E is larger than unity for pairs of elements which have a high propensity to form contacts in crystals, while pairs which tend to avoid contacts with each other yield an E value lower than unity. E values are calculated from the percentage of contacts, which, in turn, are given by the CrystalExplorer 17 software [34], between one type or two types of chemical elements in a crystal packing.

Molecular docking

Docking applications were exerted with AutoDock Vina [36] to estimate the interaction mechanisms of the compounds **1–3** as ligands with a series of COVID-19 proteins as targets. Crystal structures of the applied proteins were extracted from the RCSB Protein Data Bank [37]. The ligands and proteins were prepared by using suitable protocols of Discovery Studio 3.5 [38] for molecular docking studies as described previously [39]. The active region of the molecular docking site contains the related proteins with an active region size of 40×40×40 with 0.375 Å grid spacing. Lamarckian genetic algorithm was used to fully search for the possible conformations and binding sites. Other docking parameters were set to the software's default values. The lowest binding energy conformers along with the lowest RMSD were captured of 100 diversified conformers from the docking genetic algorithm runs. The docked poses were analyzed and visualized in Discovery Studio 3.5.

Results and discussion

The bis-*N*-salicylidene aniline dyes **1–3** (Fig. 1) are readily obtained by the condensation reaction of 1,5-diaminonaphthalene with salicylaldehyde [27], 3-hydroxysalicylaldehyde [28] and 3-methoxysalicylaldehyde [23, 28], respectively.

According to single-crystal X-ray diffraction, **1** and **3red** crystallize in monoclinic space group $P2_1/c$, while **2** and **3yellow** crystallize in triclinic $P–1$ and monoclinic $P2_1/n$ space groups, respectively [23, 27, 28]. The molecule in each structure lies on a crystallographic two-fold axis; thus, the asymmetric unit comprises one half-molecule (Fig. 2).

Notably, molecules in all the structures were found in the enol-imine form (Fig. 2). Particularly, the bond lengths of C–O, with respect to the moieties marked in bold in Fig. 1, are about 1.35 Å and those of C–C are about 1.45 Å (Table 1), which indicates single bonds, while a double bond of about 1.28 Å is revealed for C=N (Table 1). The enol-imine isomer formation is further supported by the sp^2-hybridization of both the carbon and the nitrogen atoms of the imine fragment as evidenced from the corresponding C–C=N and C=N–C bond angles, which vary from 119.64(11)° to 123.1(3)° (Table 1).

The overall shape of the discussed molecules is dictated by the corresponding dihedral angle between the least-square planes formed by the benzene and naphthalene rings. Particularly, this angle is similar in the structures of **1**, **2** and **3yellow**, which vary from 43.62(13)° to 56.37(5)° (Table 1) and is remarkably less in the structure of **3red**, 21.31(8)°. Thus, the molecule of the latter compound is much planar (Fig. 2).
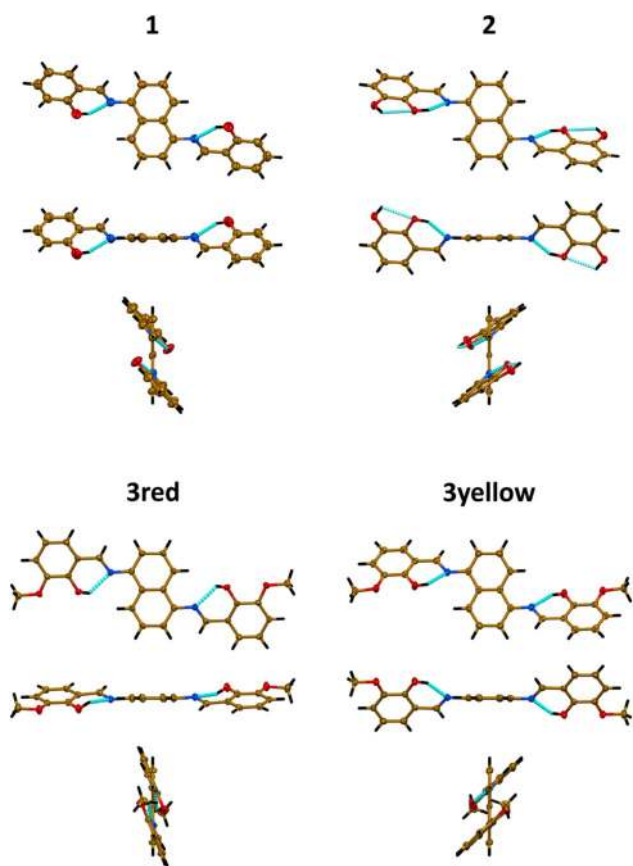
Fig. 2 Crystal structures of **1–3**. Color code: H = black, C = gold, N = blue, O = red; O–H···N hydrogen bond = dashed cyan line

The crystal structures of all molecules are stabilized by intramolecular O–H···N hydrogen bonds (Fig. 2, Table 2), yielding two six-membered hydrogen bonded pseudo-aromatic rings, which are almost perfectly planar in the structures of **1**, **2** and **3yellow**, and significantly deviated in the structure of **3red** as evidenced from the corresponding dihedral angles (Table 1). This ring is constructed from five covalent bonds and one non-covalent bond (Fig. 2), which is accompanied by certain conjugation effects and has a certain degree of covalency [40]. This is the case of the resonance-assisted hydrogen bonding (RAHB), where the donor and acceptor are connected by a π-conjugated system [41]. The aromaticity index of this pseudo-aromatic ring was found to be 0.774, 0.721, 0.747 and 0.763 for **1**, **2**, **3red** and **3yellow**, respectively, as evidenced from the Harmonic Oscillator Model of Aromaticity for Heterocycle Electron Delocalization (HOMHED) [42]. Using the same approach, the aromaticity index for the benzene rings was found to be in the range of 0.977–0.989, while the aromaticity index for the C_6H_3 rings of the naphthalene fragments was found to be 0.917–0.949, respectively. Thus, the benzene, naphthalene and, remarkably, the hydrogen bonded six-membered heterocycles are aromatic for all the discussed structures. The crystal structure of **2** is additionally stabilized by intramolecular O–H···O hydrogen bonds (Fig. 2, Table 2), yielding two five-membered hydrogen bonded heterocycles, and by intermolecular O–H···O hydrogen bonds, formed between the OH groups of adjacent molecules, yielding a 1D zig-zag supramolecular chain, comprising $R_2^2(10)$ H-bonded cycles.

Molecules of **2**, **3red** and **3yellow** are interlinked through intermolecular C–H···π interactions (Table 2). Interestingly, in the former two structures these interactions are formed

Table 1 Selected bond lengths (Å) and angles (°) in the structures of **1–3**

	1	**2**	**3red**	**3yellow**
Bond lengths				
C=N	1.283(4)	1.2824(17)	1.287(3)	1.284(2)
C–N	1.419(4)	1.4190(15)	1.417(3)	1.4152(18)
C–O	1.350(4)	1.3600(15)	1.353(3)	1.3493(18)
C–C	1.443(4)	1.4515(17)	1.454(3)	1.4486(19)
Bond angles				
C–C=N	123.1(3)	121.82(12)	121.7(2)	121.90(13)
C=N–C	120.2(3)	119.64(11)	121.24(19)	121.02(13)
Dihedral angles				
H–O–C–C	0	–4	–32	–1
O–C–C–C	0.8(5)	3.21(17)	3.3(3)	1.7(2)
C–C–C=N	–0.5(5)	–4.68(18)	–5.3(3)	2.6(2)
C–C=N···H	0	–4.5	–15.7	–4.3
C=N···H–O	–0.9	8.4	54.4	6.7
N···H–O–C	0.8	–7.3	–56.6	–3.4
$Cg_{benzene}$···$Cg_{naphthalene}$[a]	43.62(13)	56.37(5)	21.31(8)	47.04(6)

[a]Least-square planes, formed by the carbon atoms of the benzene and naphthalene rings

Table 2 Hydrogen bond and C–H···π interaction lengths (Å) and angles (°) in the structures of **1–3**[a]

	D–H···A	d(D–H)	d(H···A)	d(D···A)	$\angle$(DHA)
1	O–H···N	0.82	1.91	2.634(3)	148
2	O–H···N	0.95	1.73	2.5861(14)	149
	O–H···O	0.93	2.31	2.7335(13)	107
	O–H···O[#1]	0.93	2.02	2.8333(13)	145
3red	O–H···N	0.84	2.01	2.599(2)	126
3yellow	O–H···N	0.84	1.83	2.5981(18)	146
	C–H···O[#2]	0.98	2.52	3.213(2)	128
	C–H···O[#2]	0.98	2.59	3.564(2)	170
	C–H(I)···Cg(J)[b]	d[H(I)···Cg(J)]	d[C···Cg(J)]	$\angle$(CHCg)	γ
2	C–H···C$_6$H$_3$[#3]	2.64	3.4219(14)	140	1.86
3red	C–H···C$_6$H$_3$[#4]	2.90	3.713(3)	141	10.94
3yellow	C–H···C$_6$H$_3$[#5]	2.82	3.5895(19)	138	15.88
	C–H···C$_6$H$_{3(naphthalene)}$[#6]	2.95	3.6429(17)	130	1.54
	C–H···C$_6$H$_{3(naphthalene)}$[#7]	2.95	3.6429(17)	130	1.54
	C–H···C$_6$H$_3$[#8]	2.80	3.567(2)	135	6.26

[a]Symmetry transformations used to generate equivalent atoms: #1 $1-x$, $1-y$, $1-z$; #2 $-1/2+x$; $3/2-y$, $-1/2+z$; #3 $1-x$; $1-y$, $-z$; #4 $1-x$; $1/2+y$, $1/2-z$; #5 x; y, $1+z$; #6 $-1+x$; y, $-1+z$; #7 $1-x$; $2-y$, $1-z$; #8 $1/2+x$; $3/2-y$, $-1/2+z$

[b]H(I)···Cg(J): distance of H to ring centroid; C···Cg(J): distance of C to ring centroid; $\angle$(CHCg): C–H···Cg angle; γ: angle between Cg(J)···H(I) vector and ring J normal

with the benzene rings, while in the latter one both naphthalene six-membered rings are involved. Furthermore, the crystal packing of **1** and **2** is also described by intermolecular π···π interactions (Table 3). These interactions are formed exclusively between the benzene rings in the structure of **2**, whereas both the benzene and naphthalene rings are involved in the structure of **1**.

Crystal packing of **1**, **2**, **3red** and **3yellow** was further studied by a Hirshfeld surface analysis [32], also reflected in a set of corresponding 2D fingerprint plots [33], which were generated using CrystalExplorer 17 [34]. Additionally, the enrichment ratios (E) [35] of the intermolecular contacts were also calculated to estimate the propensity of two chemical species to be in contact. It was found that the Hirshfeld surfaces of **1**, **2** and **3red**, calculated over d_{norm}, each contain two symmetrical pairs of bright red spots, corresponding to donors and acceptors of the C–H···C (in **1**), O–H···O (in **2**), C–H···H–C and C–H···C (in **3red**) intermolecular interactions (Fig. 3). The same surface of **3yellow** contains ten symmetrical pairs of bright red spots, corresponding to donors and acceptors of the C–H···O, C···C and C–H···C intermolecular interactions (Fig. 3). The donors and the acceptors of these interactions can be evidenced as blue and red regions around the participating atoms on the Hirshfeld surface mapped over shape index (Fig. 3). Moreover, flat regions were observed over both sides of the benzene and naphthalene rings on the Hirshfeld surface of **1**, mapped over curvedness, testifying to the reasonable π···π interactions (Fig. 3). Similar flat regions were found over one side of the

benzene rings on the Hirshfeld surface of **2**, also testifying to the reasonable π···π interactions (Fig. 3).

It was further found that more than 90% of the total Hirshfeld surface are for all the discussed molecules is occupied by H···H, H···C, H···O and C···C contacts (Table 4). However, the distribution of these contacts within each molecule differs significantly, which is, obviously, due to the presence of additional OH and MeO groups in the structures of **2**, and **3red** and **3yellow**, respectively. At the same time, we herein discuss two polymorphs **3red** and **3yellow**, which are chemically the same but differ geometrically (Fig. 2, Tables 1 and 2), thus yielding remarkably different Hirshfeld surfaces.

According to the Hirshfeld surface analysis of **1**, the intermolecular H···H, H···C, H···O and C···C contacts comprise about 52%, 18%, 10% and 14% of the total number of contacts (Table 4). Incorporation of two additional OH groups in a molecule, yielding the structure of **2**, significantly decreases proportions of the H···H (~38%) and C···C (~5%) contacts simultaneously increasing proportions of the H···C (~35%) and H···O (~18%) contacts (Table 4). This can be explained by the formation of O–H···O intermolecular hydrogen bonds (Table 2) in the crystal structure of **2** together with a superior propensity of **1** to produce π···π intermolecular interactions (Table 3). Substitution of two *meta*-OH groups by two MeO groups, yielding the structure of **3red**, increases a proportion of the intermolecular H···H contacts (~46%) on the Hirshfeld surface area, which is now compatible with **1** (~52%), accompanied with a dramatic decreasing of a proportion of the H···C contacts (~24%).

Table 3 $\pi\cdots\pi$ distances (Å) and angles (°) for **1** and **2**[a]

	Cg(I)	Cg(J)	d[Cg(I)$\cdots$Cg(J)]	α	β	γ	Slippage	Symmetry operation
1	C_6H_4	C_6H_4	3.851(2)	0.02(16)	26.5	26.5	1.719	$-1+x, y, z$
	C_6H_4	C_6H_4	3.851(2)	0.02(16)	26.5	26.5	1.719	$1+x, y, z$
	C_6H_3	C_6H_3	3.851(2)	0.00(14)	27.3	27.3	1.766	$-1+x, y, z$
	C_6H_3	C_6H_3	3.851(2)	0.00(14)	27.3	27.3	1.766	$1+x, y, z$
	C_6H_3	C_6H_3	3.647(2)	0.00(14)	20.2	20.2	1.258	$1-x, 1-y, -z$
	C_6H_3	C_6H_3	3.647(2)	0.00(14)	20.2	20.2	1.258	$1+x, y, z$
	C_6H_3	C_6H_3	3.851(2)	0.00(14)	27.3	27.3	1.766	$-1-x, 1-y, -z$
	C_6H_3	C_6H_3	3.851(2)	0.00(14)	27.3	27.3	1.766	$1-x, 1-y, -z$
	C_6H_3	$C_{10}H_6$	3.549(2)	0.05(12)	15.3	15.3	0.936	$1+x, y, z$
	C_6H_3	$C_{10}H_6$	3.549(2)	0.05(12)	15.3	15.3	0.936	$1-x, 1-y, -z$
	C_6H_3	C_6H_3	3.647(2)	0.00(14)	20.2	20.2	1.258	$-1+x, y, z$
	C_6H_3	C_6H_3	3.851(2)	0.00(14)	27.3	27.3	1.766	$-1-x, 1-y, -z$
	C_6H_3	C_6H_3	3.851(2)	0.00(14)	27.3	27.3	1.766	$1-x, 1-y, -z$
	C_6H_3	C_6H_3	3.851(2)	0.00(14)	27.3	27.3	1.766	$-1+x, y, z$
	C_6H_3	C_6H_3	3.851(2)	0.00(14)	27.3	27.3	1.766	$1+x, y, z$
	C_6H_3	C_6H_3	3.647(2)	0.00(14)	20.2	20.2	1.258	$-1-x, 1-y, -z$
	C_6H_3	$C_{10}H_6$	3.549(2)	0.05(12)	15.3	15.3	0.936	$-1+x, y, z$
	C_6H_3	$C_{10}H_6$	3.549(2)	0.05(12)	15.3	15.3	0.936	$-1-x, 1-y, -z$
	$C_{10}H_6$	C_6H_3	3.548(2)	0.05(12)	15.3	15.3	0.934	$-1+x, y, z$
	$C_{10}H_6$	C_6H_3	3.548(2)	0.05(12)	15.3	15.3	0.934	$1-x, 1-y, -z$
	$C_{10}H_6$	C_6H_3	3.548(2)	0.05(12)	15.3	15.3	0.934	$1+x, y, z$
	$C_{10}H_6$	C_6H_3	3.548(2)	0.05(12)	15.3	15.3	0.934	$-1-x, 1-y, -z$
	$C_{10}H_6$	$C_{10}H_6$	3.851(2)	0.02(9)	27.3	27.3	1.764	$-1+x, y, z$
	$C_{10}H_6$	$C_{10}H_6$	3.851(2)	0.02(9)	27.3	27.3	1.764	$1+x, y, z$
	$C_{10}H_6$	$C_{10}H_6$	3.851(2)	0.02(9)	27.3	27.3	1.764	$-1-x, 1-y, -z$
	$C_{10}H_6$	$C_{10}H_6$	3.851(2)	0.02(9)	27.3	27.3	1.764	$1-x, 1-y, -z$
2	$C_6H_{3(benzene)}$	$C_6H_{3(benzene)}$	4.0348(8)	0.00(6)	34.6	34.6	2.290	$-x, 1-y, 1-z$

[a]Cg(I)$\cdots$Cg(J): distance between ring centroids; α: dihedral angle between planes Cg(I) and Cg(J); β: angle Cg(I)$\rightarrow$Cg(J) vector and normal to plane I; γ: angle Cg(I)$\rightarrow$Cg(J) vector and normal to plane J; slippage: distance between Cg(I) and perpendicular projection of Cg(J) on ring I

Fig. 3 Molecular Hirshfeld surfaces of **1–3** (top, middle and bottom denote normalized distance dnorm, shape index and curvedness, respectively)
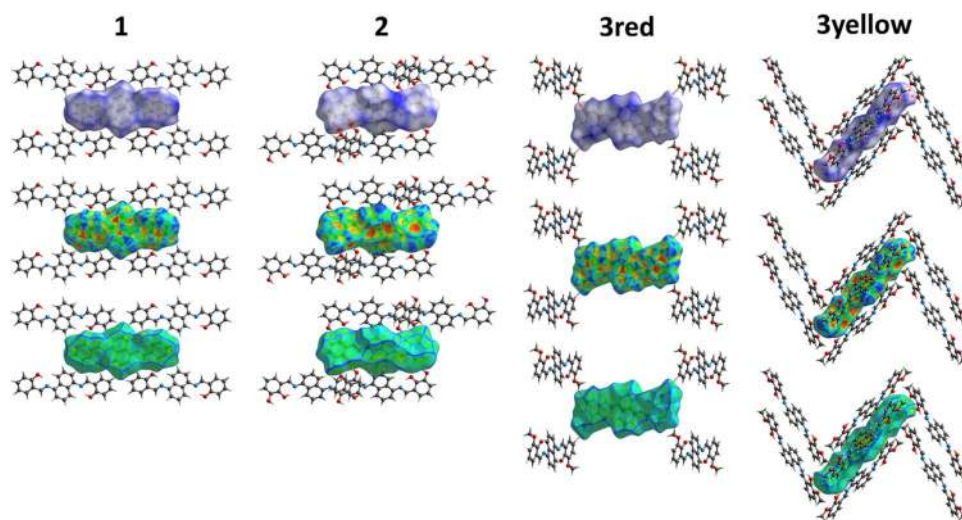
Table 4 Hirshfeld contact surfaces and derived "random contacts" and "enrichment ratios" for **1–3**

	1				2				3red				3yellow			
	H	C	N	O	H	C	N	O	H	C	N	O	H	C	N	O
Contacts (C, %)[a]																
H	51.8	–	–	–	37.9	–	–	–	45.9	–	–	–	37.6	–	–	–
C	18.1	14.4	–	–	35.3	4.9	–	–	24.1	6.7	–	–	39.2	1.7	–	–
N	1.3	2.0	0.2	–	1.1	0.6	0.0	–	0.0	5.0	0.0	–	2.8	0.0	0.0	–
O	10.4	1.3	0.2	0.2	17.9	2.4	0.0	0.0	16.6	1.7	0.0	0.0	18.1	0.6	0.0	0.0
Surface (S, %)																
	66.7	25.1	2.0	6.2	65.1	24.1	0.9	10.2	66.3	22.1	2.5	9.2	67.7	21.6	1.4	9.4
Random contacts (R, %)																
H	44.5	–	–	–	42.4	–	–	–	44.0	–	–	–	45.8	–	–	–
C	33.5	6.3	–	–	31.4	5.8	–	–	29.3	4.9	–	–	29.2	4.7	–	–
N	2.7	0.3	0.0	–	1.2	0.1	0.0	–	3.3	0.2	0.1	–	1.9	0.1	0.0	–
O	8.3	3.1	0.2	0.4	13.3	4.9	0.2	1.0	12.2	4.1	0.5	0.8	12.7	4.1	0.3	0.9
Enrichment (E)[b]																
H	1.16	–	–	–	0.89	–	–	–	1.04	–	–	–	0.82	–	–	–
C	0.54	2.29	–	–	1.12	0.84	–	–	0.82	1.37	–	–	1.34	0.36	–	–
N	0.48	–	–	–	0.92	–	–	–	0.00	–	–	–	1.47	–	–	–
O	1.25	0.42	–	–	1.35	0.49	–	–	1.36	0.41	–	–	1.43	0.15	–	–

[a]Values were obtained from CrystalExplorer 17 [34]

[b]The "enrichment ratios" were not computed when the "random contacts" were lower than 0.9%, as they are not meaningful [35]

Notably, while proportions of the H···O (~17%) and C···C (~7%) contacts in the structure of **3red** are very similar to those in the structure of **2**, a new type of intermolecular contacts, namely C···N contacts (5%), also comes to the fore on the Hirshfeld surface of **3red** (Table 4). This can be explained by a much more planar structure of **3red** in comparison with the other discussed molecules (Fig. 2, Table 1). Interestingly, the intermolecular H···H, H···C and H···O contacts in the Hirshfeld surface of **3yellow** each comprise similar proportions as in the surface of **2** (Table 4). It should also be noted that proportions of the H···H and H···C contacts in **2** and **3yellow** are not only pairwise similar but also very similar within each structure, varying from ~35 to ~39% (Table 4).

The shortest H···H, H···C and H···O contacts are shown in the corresponding fingerprint plots at $d_e + d_i \approx$ 2.1–2.4, 2.7–2.9 and 2.0–2.7 Å, respectively (Fig. 4). A subtle feature is evident in the fingerprint plots of **2** and **3red**, namely a splitting of the short H···H fingerprint (Fig. 4). This splitting occurs when the shortest contact is between three atoms, rather than for a direct two-atom contact [32]. Notably, in the fingerprint plots of **2**, **3red** and **3yellow** the H···C contacts are shown in the form of "wings" (Fig. 4) and are recognized as characteristic of C–H···π nature [33], while the H···O contacts in the fingerprint plot of **2** are shown as a pair of sharp spikes (Fig. 4) due to the formation of strong intermolecular O–H···O hydrogen bonds (Table 2). Furthermore, the H···C contacts are shown in the fingerprint plots as

the characteristic area on the diagonal at $d_e = d_i \approx$ 1.7–2.2 Å (Fig. 4) and correspond π···π interactions.

Despite that all structures are characterized by almost the same values of $S_{C/H/N/O}$ and random contacts $R_{XX/XY}$, the H···H and C···C contacts are highly favored only in the structures of **1** and **3red** since the corresponding enrichment ratios E_{HH} and E_{CC} are larger than unity, while the same contacts are less favored or even impoverished in the structures of **2** and **3yellow** as evidenced from the corresponding E_{HH} and E_{CC} values being less than unity (Table 4). The opposite trend is observed for the H···C contacts, which are highly favored in the structures of **2** and **3yellow** and diminished in the structures of **1** and **3red** (Table 4). Notably, the H···O contacts are highly enriched in all the discussed structures, while the H···N contacts are favored only in the structure of **3yellow** (Table 4).

Voids in the crystal structures of the discussed compounds (Fig. 5) were calculated using CrystalExplorer 17 [34]. It was found that the void volumes are 60.21, 51.89, 99.12 and 108.22 Å^3 in **1**, **2**, **3red** and **3yellow**, respectively, with the corresponding surface areas of 259.00, 152.45, 309.93 and 371.29 Å^2. With the porosity, the calculated void volumes of **1**, **2**, **3red** and **3yellow** are about 7%, 11%, 10% and 10%, respectively. Thus, molecules are more tightly packed in the crystal structure of **1**. This might be explained by a rich variety of intermolecular π···π interactions, which are formed due to all aromatic rings, comprising the molecule of **1**.
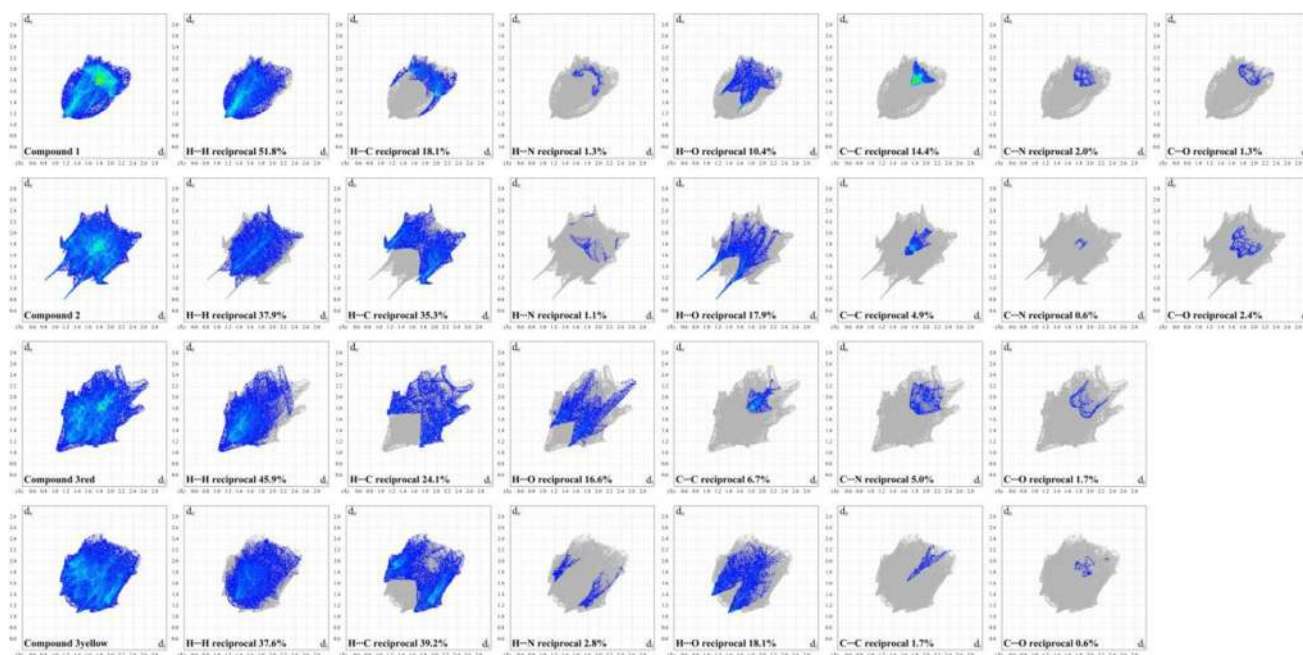
Fig. 4 2D and decomposed 2D fingerprint plots of observed contacts for **1–3**. The decomposed 2D fingerprint plots of the N···N (0.2%), N···O (0.2%) and O···O (0.2%) contacts for **1** are not shown for clarity
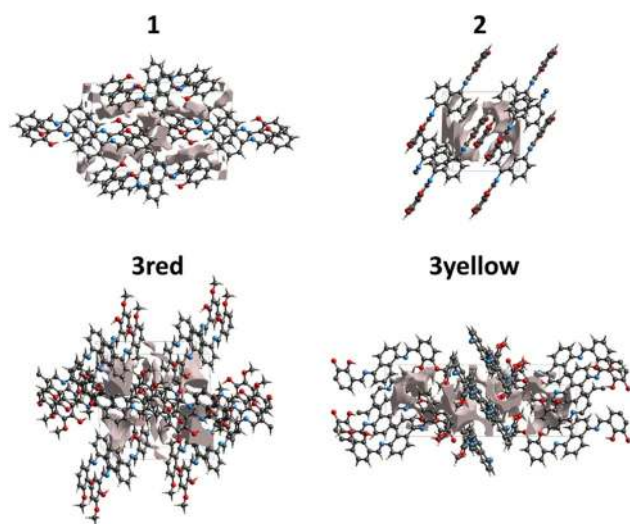
Fig. 5 Void plots for **1–3** (results under 0.002 a. u. isovalue)

We have also calculated energy frameworks [43] using CrystalExplorer 17 [34] to further analyze the crystal packing of **1**, **2**, **3red** and **3yellow** (Table 5, Fig. 6). The overall topology of the energy distributions in the discussed crystal structures was studied through the energy framework. It was established that the structures are mainly characterized by the dispersion energy framework followed by the less significant electrostatic energy framework contribution (Fig. 7).

We have also examined evaluation of the biological efficacy of **1–3** against of a series of the SARS-CoV-2 proteins

(Table 6) using the molecular docking approach. Note that we used the structure of **3red** as a general representative of both polymorphs of **3**.

It was established that the predicted binding energies of **1–3** show high binding affinity with the four proteins, namely Papain-like protease (PLpro), nonstructural protein 3 (nsp3_range 207–379-MES), RdRp-RTR and Nsp14 (N7-MTase) (marked by bold in Table 6). Both **1** and **3** exhibit the best interaction with the latter protein, while **2** is more efficient toward the first protein.

These findings are explained by different sets of intermolecular interactions formed between **1** and **3** and corresponding proteins revealed from the molecular docking studies. Particularly, the main interactions between **1** and Nsp14 (N7-MTase) are one conventional hydrogen bond with ASP352, one carbon hydrogen bond with Asn386, one S···π-system interaction with Cys387, two π···π interactions with Ph3367 and Phe426, and three alkyl···π-system interactions with Val290 and Ala353, respectively (Fig. 8, Table S1 in the Supplementary Information).

The interaction of **2** with PLpro is described by two conventional hydrogen bonds with Asp164 and Thr301, one carbon hydrogen bond with Tyr268, one cation···π-system interaction with Lys157, one anion···π-system interaction with Glu161, two π···π interactions with Tyr264 and Tyr207, and two alkyl···π-system interactions with Leu162 and Pro248 (Fig. 9, Table S1 in the Supplementary Information).

Finally, **3**, similar to **1**, exhibits the best interaction with Nsp14 (N7-MTase), however with 0.2 kcal/mol lower

Table 5 Interaction energies (kJ/mol) calculated at the B3LYP/6-31G(d,p) theory level for the crystal structures of **1–3**.[a] Values in parenthesis are obtained after normalizing to 100% the sum of the attractive energy contributions

		N	symmetry operation	R	E_{ele}[b]	E_{pol}[b]	E_{dis}[b]	E_{rep}[b]	E_{tot}[b]
1	red	4	$-x, y + 1/2, -z + 1/2$	11.35	−3.7 (12.1)	−1.5 (4.9)	−25.3 (83.0)	15.7	−17.3
	yellow	2	x, y, z	19.77	0.0 (0.0)	−0.3 (3.8)	−7.5 (96.2)	4.9	−3.8
	green	2	x, y, z	3.85	−6.1 (4.5)	−3.2 (2.4)	−126.6 (93.1)	70.6	−75.5
	cyan	4	$-x, y + 1/2, -z + 1/2$	11.79	−6.1 (25.2)	−1.4 (5.8)	−16.7 (69.0)	12.1	−14.7
	blue	4	$-x, y + 1/2, -z + 1/2$	12.18	−0.7 (8.1)	−0.2 (2.3)	−7.7 (89.6)	4.1	−5.1
	magenta	2	x, y, z	20.87	−0.1 (6.3)	0.0 (0.0)	−1.5 (93.7)	0.0	−1.4
2	red	2	x, y, z	6.28	−11.2 (18.0)	−1.9 (3.1)	−49.1 (78.9)	30.3	−37.3
	orange	2	x, y, z	8.65	−9.0 (16.2)	−1.5 (2.7)	−44.9 (81.1)	33.2	−29.2
	green	2	x, y, z	8.75	−6.2 (11.8)	−1.2 (2.3)	−45.3 (85.9)	23.7	−32.3
	cyan	2	x, y, z	12.61	−14.9 (19.0)	−2.9 (3.7)	−60.5 (77.3)	42.2	−44.5
	blue	2	x, y, z	18.86	−6.5 (34.6)	−1.6 (8.5)	−10.7 (56.9)	11.1	−10.5
	dark blue	2	x, y, z	19.60	−0.8 (10.3)	0.0 (0.0)	−7.0 (89.7)	3.9	−4.6
	magenta	2	x, y, z	13.10	−38.0 (68.7)	−1.9 (3.4)	−15.4 (27.9)	42.5	−28.8
3red	red	4	$-x, y + 1/2, -z + 1/2$	7.79	−4.0 (18.7)	−1.6 (7.5)	−15.8 (73.8)	6.4	−15.3
	orange	4	$-x, y + 1/2, -z + 1/2$	10.58	−9.0 (30.1)	−2.3 (7.7)	−18.6 (62.2)	12.6	−19.7
	green	2	x, y, z	5.07	−11.3 (9.4)	−2.4 (2.0)	−106.4 (88.6)	50.9	−74.9
	green2	4	$-x, y + 1/2, -z + 1/2$	14.95	−4.4 (12.8)	−4.4 (12.8)	−25.7 (74.4)	18.6	−18.8
	cyan	2	x, y, z	17.31	−1.6 (15.0)	0.0 (0.0)	−9.1 (85.0)	4.9	−6.6
	blue	2	x, y, z	21.18	−0.7 (28.0)	−0.1 (4.0)	−1.7 (68.0)	0.1	−2.2
	purple	4	$-x, y + 1/2, -z + 1/2$	14.65	−1.6 (12.5)	−0.5 (3.9)	−10.7 (83.6)	13.2	−3.2
	magenta	2	x, y, z	20.69	0.5	0.0 (0.0)	−0.9 (100.0)	0.0	−0.3
3yellow	red	2	x, y, z	7.58	−9.6 (13.5)	−6.6 (9.3)	−54.7 (77.2)	22.9	−48.5
	yellow	2	x, y, z	6.74	−5.0 (8.2)	−5.1 (8.4)	−50.7 (83.4)	33.3	−32.7
	green	2	x, y, z	6.87	−15.4 (16.0)	−1.6 (1.7)	−79.5 (82.3)	56.6	−51.7
	blue	4	$-x + 1/2, y + 1/2, -z + 1/2$	12.68	−11.2 (35.2)	−0.3 (0.9)	−20.3 (63.9)	19.8	−17.4
	purple	4	$-x + 1/2, y + 1/2, -z + 1/2$	13.36	−3.3 (18.8)	−0.1 (0.6)	−14.2 (80.6)	10.1	−9.8

[a] N is the number of molecules with an R molecular centroid-to-centroid distance (Å); color codes in the first column are referenced to Fig. 6

[b] E_{ele} is the electrostatic energy, E_{pol} is the polarization energy, E_{dis} is the dispersion energy, E_{rep} is the exchange-repulsion energy, k values are scale factors; $E_{tot} = k_{ele} \times E_{ele} + k_{pol} \times E_{pol} + k_{dis} \times E_{dis} + k_{rep} \times E_{rep} = 1.057 \times E_{ele} + 0.740 \times E_{pol} + 0.871 \times E_{dis} + 0.618 \times E_{rep}$ [43]
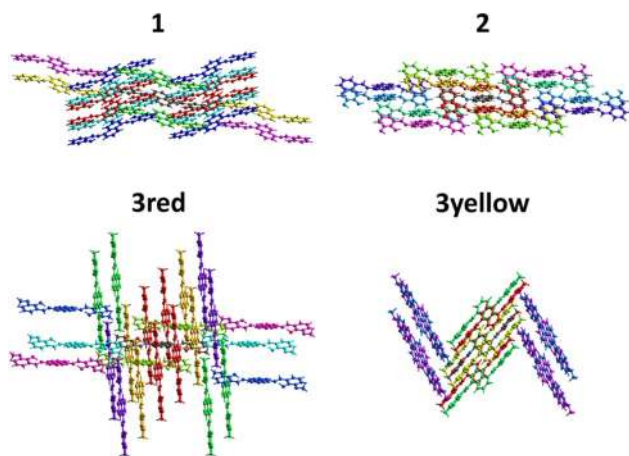

Fig. 6 The color-coded interaction mapping within 3.8 Å of the centring molecule in the crystal structures of **1–3**, calculated from a single-point molecular wavefunction at B3LYP/6-31G(d,p)

binding energy, which is, most likely, due to steric effects (Fig. 10, Table 6). Compound **1** interacts with Nsp14 (N7-MTase) through three conventional hydrogen bonds with Arg310 and Ala353, five carbon bonds with Gly333, Asn386, Asn306 and Leu366, one $\sigma \cdots \pi$ interaction with Val290, one S$\cdots \pi$-system interaction with Cys387, two $\pi \cdots \pi$ interactions with Phe367 and Phe426, and one alkyl$\cdots \pi$-system interaction with Ala353 (Fig. 9, Table S1 in the Supplementary Information).

Conclusions

In summary, we report detailed structural studies of an extremely rare family of naphthalene-based bis-*N*-salicylidene aniline dyes, namely *N,N′*-bis-salicylidene-1,5-diaminonaphthalene (**1**), *N,N′*-bis(3-hydroxysalicylidene)-1,5-diaminonaphthalene (**2**) and *N,N′*-bis(3-methoxysalicylidene)-1,5-diaminonaphthalene (**3**).

Fig. 7 Energy frameworks calculated for the crystal structures of **1–3**, showing the electrostatic potential force (red), dispersion force (green) and total energy diagrams (blue). The cylindrical radii are proportional to the relative strength of the corresponding energies and they were adjusted to the same scale factor of 200 with a cut-off value of 5 kJ/mol for **1**, **2** and **3yellow**, and 3 kJ/mol for **3red** within 2×2×3 unit cells
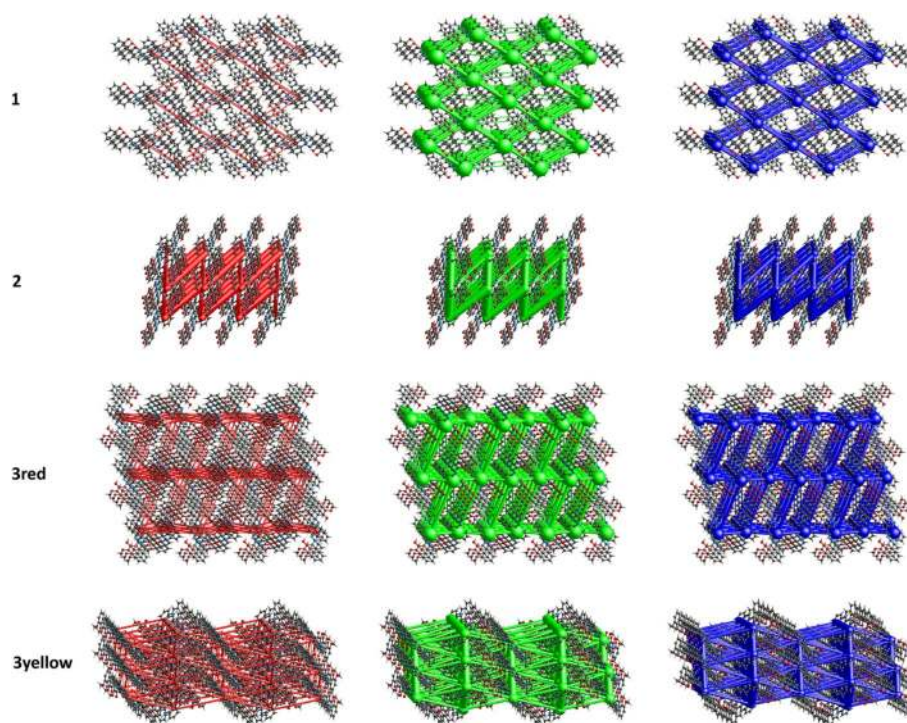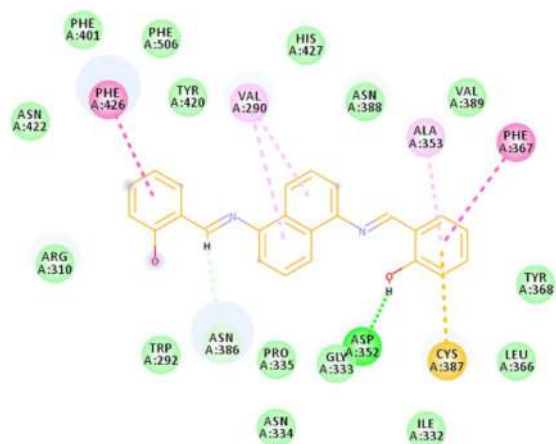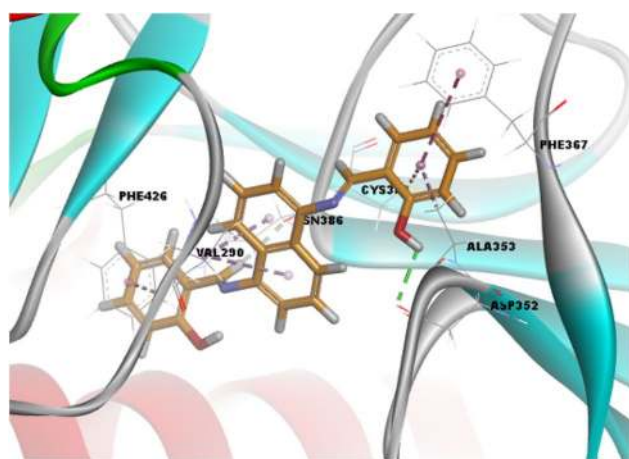

Table 6 The best poses of **1–3** inside the binding sites of the listed proteins

Protein	PDB code	Binding energy (kcal/mol)		
		1	**2**	**3**
Main protease (Mpro)	6LU7	−8.30	−8.00	−7.60
Papain-like protease (PLpro)	6WUU	**−9.70**	**−10.40**	**−9.20**
Nonstructural protein 3 (nsp3_range 207−379-AMP)	6W6Y	−8.00	−8.10	−7.90
Nonstructural protein 3 (nsp3_range 207–379-MES)	6W6Y	**−9.50**	**−9.30**	**−9.10**
Helicase (Nsp13)-adp	6JYT	−7.80	−7.80	−7.90
Helicase (Nsp13)-ncb	6JYT	−8.20	−8.50	−8.10
RdRp-RTR	7BV2	**−9.40**	**−9.70**	**−9.30**
RdRp-RNA	7BV2	−7.80	−8.10	−7.70
Nsp14 (ExoN)	5C8S	−7.40	−7.40	−7.40
Nsp14 (N7-MTase)	5C8S	**−9.90**	**−10.10**	**−9.70**
Nsp15 (endoribonuclease)	6WLC	−8.00	−8.00	−7.80
Nsp16 (GTA site)	6WVN	−8.50	−8.50	−8.80
Nsp16 (MGP site)	6WVN	−7.90	−7.90	−8.00
Nsp16 (SAMsite)	6WVN	−8.80	−8.90	−8.80
N protein (NCB site)	6WXD	−8.20	−8.00	−8.10

The Schiff base **3** exists as two polymorphs, herein named as **3red** and **3yellow**. Both polymorphs of **3** were analyzed and discussed.

Single-crystal X-ray diffraction revealed that all the discussed molecules lie on a crystallographic two-fold axis; thus, the asymmetric unit comprises one half-molecule exhibiting an enol-imine tautomer, stabilized by a couple of intramolecular O–H···N hydrogen bonds. The structure of **2** is further stabilized by a couple of additional O–H···O intramolecular hydrogen bonds and by intermolecular O–H···O interactions, yielding a 1D zig-zag supramolecular chain. Molecules of **2**, **3red** and **3yellow** are interlinked through intermolecular C–H···π interactions, while the crystal
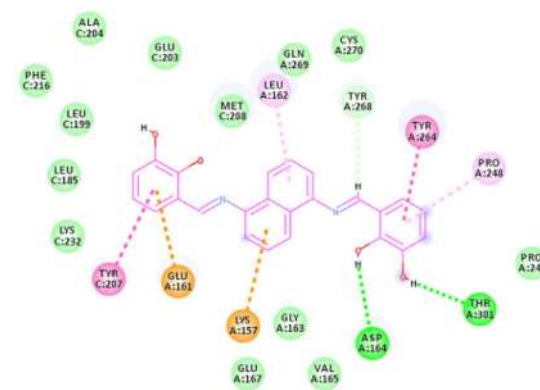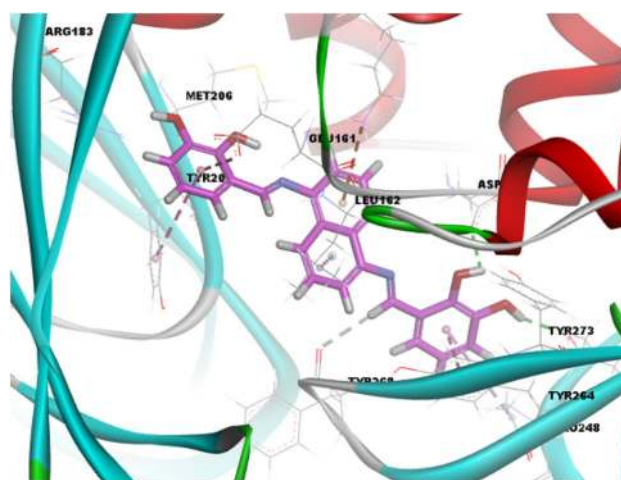
Fig. 8 3D (top) and 2D (bottom) views on the interaction of **1** with Nsp14 (N7-MTase)

Fig. 9 3D (top) and 2D (bottom) views on the interaction of **2** with PLpro

packing of **1** and **2** is also described by intermolecular $\pi\cdots\pi$ interactions.

It was established that more than 90% of the total Hirshfeld surface area for all the discussed molecules is occupied by H$\cdots$H, H$\cdots$C, H$\cdots$O and C$\cdots$C contacts. However, the distribution of these contacts within each molecule differs significantly, which is, obviously, due to the presence of additional OH and MeO groups in the structures of **2**, and **3red** and **3yellow**, respectively. Notably, two polymorphs **3red** and **3yellow**, despite being chemically the same, differ geometrically, thus yielding remarkably different Hirshfeld surfaces. In general, the Hirshfeld surface of **3yellow** is very similar to that of **2**.

Energy frameworks have been calculated to additionally analyze the overall crystal packing. It was established that

the all the structures are mainly characterized by the dispersion energy framework followed by the less significant electrostatic energy framework contribution.

The molecular docking studies were performed to elucidate the effects of **1–3** on to reveal the binding mechanisms of a series of the SARS-CoV-2 proteins. Docking results revealed that **1–3** show high binding affinity with Papain-like protease (PLpro), nonstructural protein 3 (nsp3_range 207–379-MES) and RdRp-RTR and Nsp14 (N7-MTase). Both **1** and **3** exhibit the best interaction with the latter protein, while **2** is more efficient toward the first protein.

Finally, we hope that the results reported herein will be of value for future design of potential chemicals against SARS-CoV-2.
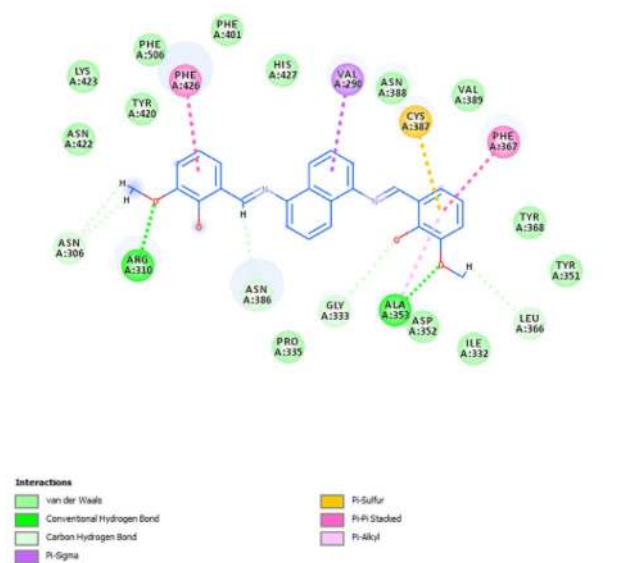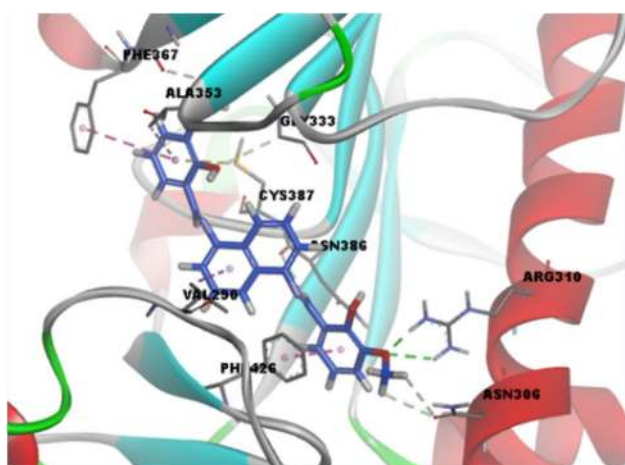
Fig. 10 3D (top) and 2D (bottom) views on the interaction of **3** with Nsp14 (N7-MTase)

Declarations

Conflict of interest The authors declared that they have no conflicts of interest in this work.

References

1. H. Schiff, Eur. J. Org. Chem. **131**, 118–119 (1864)
2. IUPAC in *Compendium of Chemical Terminology*, 2nd ed. (the "Gold Book"), ed. by A.D. McNaught, A. Wilkinson (Blackwell Scientific Publications, Oxford, 1997)
3. https://goldbook.iupac.org/terms/view/A00357
4. E. Hadjoudis, M. Vitterakis, I. Moustakali, I. Mavridis, Tetrahedron **43**, 1345–1360 (1987)
5. E. Hadjoudis, I.M. Mavridis, Chem. Soc. Rev. **33**, 579–588 (2004)
6. K. Amimoto, T. Kawato, J. Photochem. Photobiol. C **6**, 207–226 (2005)
7. T. Haneda, M. Kawano, T. Kojima, M. Fujita, Angew. Chem. Int. Ed. **46**, 6643–6645 (2007)
8. A. Filarowski, A. Koll, L. Sobczyk, Curr. Org. Chem. **13**, 172–193 (2009)
9. V. Bertolasi, P. Gilli, G. Gilli, Curr. Org. Chem. **13**, 250–268 (2009)
10. E. Hadjoudis, S.D. Chatziefthimiou, I.M. Mavridis, Curr. Org. Chem. **13**, 269–286 (2009)
11. V.I. Minkin, A.V. Tsukanov, A.D. Dubonosov, V.A. Bren, J. Molec. Struct. **998**, 179–191 (2011)
12. Y. Inokuma, M. Kawano, M. Fujita, Nat. Chem. **3**, 349–358 (2011)
13. K.T. Mahmudov, A.J.L. Pombeiro, Chem. Eur. J. **22**, 16356–16398 (2016)
14. C. Bertarellia, A. Biancoc, R. Castagnaa, G. Pariania, J. Photochem. Photobiol. C **12**, 106–125 (2011). (**and references therein**)
15. P. Bamfield, M.G. Hutchings, *Chromic Phenomena: Technological Applications of Colour Chemistry* (Royal Society of Chemistry, Cambridge, 2010)
16. D.A. Safin, K. Robeyns, Y. Garcia, CrystEngComm **14**, 5523–5529 (2012)
17. D.A. Safin, K. Robeyns, Y. Garcia, RSC Adv. **2**, 11379–11388 (2012)
18. D.A. Safin, Y. Garcia, RSC Adv. **14**, 6466–6471 (2013)
19. D.A. Safin, M. Bolte, Y. Garcia, CrystEngComm **16**, 5524–5526 (2014)
20. D.A. Safin, M.G. Babashkina, K. Robeyns, M. Bolte, Y. Garcia, CrystEngComm **16**, 7053–7061 (2014)
21. D.A. Safin, M. Bolte, Y. Garcia, CrystEngComm **16**, 8786–8793 (2014)
22. D.A. Safin, M.G. Babashkina, K. Robeyns, Y. Garcia, RSC Adv. **16**, 53669–53678 (2016)
23. D.A. Safin, K. Robeyns, M.G. Babashkina, Y. Filinchuk, A. Rotaru, C. Jureschi, M.P. Mitoraj, J. Hooper, M. Brela, Y. Garcia, CrystEngComm **16**, 7249–7259 (2016)
24. D.A. Safin, K. Robeyns, Y. Garcia, CrystEngComm **18**, 7284–7296 (2016)
25. A.A. Shiryaev, T.M. Burkhanova, G. Mahmoudi, M.G. Babashkina, D.A. Safin, J. Lumin. **226**, 117454 (2020)
26. D.S. Shapenova, A.A. Shiryaev, M. Bolte, M. Kukułka, D.W. Szczepanik, J. Hooper, M.G. Babashkina, G. Mahmoudi, M.P. Mitoraj, D.A. Safin, Chem. Eur. J. **26**, 12987–12995 (2020)
27. S. Karthikeyan, J. Muthukumaran, R. Krishna, B. Manimaran, Acta Crystallog. **E67**, o1765–o1766 (2011)
28. G. Ceyhan, M. Köse, V. McKee, S. Uruş, A. Gölcü, M. Tümer, Spectrochim. Acta A **95**, 382–398 (2012)
29. C.R. Groom, I.J. Bruno, M.P. Lightfoot, S.C. Ward, Acta Crystallogr. B **72**, 171–179 (2016)
30. M.M. Belmonte, E.C. Escudero-Adan, J. Benet-Buchholz, R.M. Haak, A.W. Kleij, Eur. J. Org. Chem. **2010**, 4823–4831 (2010)

31. P.-H. Wang, J.G. Keck, E.J. Lien, M.M.C. Lai, J. Med. Chem. **33**, 608–614 (1990)
32. M.A. Spackman, D. Jayatilaka, CrystEngComm **11**, 19–32 (2009)
33. M.A. Spackman, J.J. McKinnon, CrystEngComm **4**, 378–392 (2002)
34. M.J. Turner, J.J. McKinnon, S.K. Wolff, D.J. Grimwood, P.R. Spackman, D. Jayatilaka, M.A. Spackman, CrystalExplorer17, University of Western Australia, 2017, http://hirshfeldsurface.net
35. C. Jelsch, K. Ejsmont, L. Huder, IUCrJ **1**, 119–128 (2014)
36. O. Trott, A.J. Olson, J. Comput. Chem. **31**, 455–461 (2010)
37. Protein Data Bank. Available online: https://www.rcsb.org/
38. Accelrys Software Inc. Discovery Studio Modeling Environment, Release 3.5 Accelrys Software Inc, San Diego (2013)
39. E. Aki-Yalcin, T. Ertan-Bolelli, T. Taskin-Tok, O. Ozturk, S. Ataei, C. Ozen, I. Yildiz, I. Yalcin, SAR QSAR Environ. Res. **25**, 637–649 (2014)
40. L. Sobczyk, S.J. Grabowski, T.M. Krygowski, Chem. Rev. **105**, 3513–3560 (2005)
41. C.P. Frizzo, M.A.P. Martins, Struct. Chem. **23**, 375–380 (2012)
42. T.M. Krygowski, K. Woźniak, R. Anulewicz, D. Pawlak, W. Kolodziejski, E. Grech, A. Szady, J. Phys. Chem. A **101**, 9399–9404 (1997)
43. C.F. Mackenzie, P.R. Spackman, D. Jayatilaka, M.A. Spackman, IUCrJ **4**, 575–587 (2017)